Large-scale aseismic motion identified through 4-D P-wave tomography

Marco Calo', Catherine Dorbath, François Cornet, Nicolas Cuenot

Geophysical Journal International

Geophys. J. Int. (2011) **186,** 1295–1314 doi: 10.1111/j.1365-246X.2011.05108.x

Large-scale aseismic motion identified through 4-D *P*-wave tomography

M. Calò,[1] C. Dorbath,[1,2] F.H. Cornet[3] and N. Cuenot[4]

[1] *Ecole et Observatoire des Sciences de la Terre, EOST, University of Strasbourg, Strasbourg Cedex, France. E-mail: calo@unistra.fr*
[2] *GET (IRD-UMR234)*
[3] *Institut de Physique du Globe de Strasbourg (CNRS-UMR7516),* 67084 *Strasbourg Cedex, France*
[4] *GEIE, France*

Accepted 2011 June 6. Received 2011 June 6; in original form 2010 November 11

SUMMARY

In 2000, a large water injection (over 23 000 m^3) has been conducted in granite through a 5-km-deep borehole at Soultz-sous–Forêts, in the Upper Rhine Graben (northeastern France). The microseismicity induced by this hydraulic stimulation was monitored with a network of 14 seismic stations deployed at ground surface. Some 7215 well-located events have been used to conduct a 4-D tomography of *P*-wave velocities. The method combines a double-difference tomography method with an averaging post-processing that corrects for parameter dependence effects. The total set of 7 215 events has been divided into 14 subsets that explore periods defined with respect to the injection scheme. Particular attention is given to changes in injected flow rates, periods of stationary injection conditions and post-injection periods. Fast changes in V_P velocities are identified in large rock mass volumes precisely when the injection flow rate varies while little velocity variation is detected during stationary injection periods. The V_P anomalies observed during stationary injection conditions are interpreted as being caused by effective stress variations linked to fluid diffusion, while the fast changes observed concomitantly to changes in flow rate are considered to be caused by non-seismic motions.

Key words: Hydrogeophysics; Seismic tomography; Rheology and friction of fault zones; Intra-plate processes.

INTRODUCTION

Exploitation of geothermal energy from hot dry rocks (HDR) at depths of several kilometres has been the goal of various projects since the mid-1970s. A European HDR project was initiated at Soultz-sous-Forêts (Alsace, France) in 1987 (Gérard & Kappelmeyer 1987; Kappelmeyer *et al*. 1991) but was renamed later 'Enhanced Geothermal System' (EGS) after it was established that the fractured granite at Soultz was not dry but contained large volumes of hot saline fluid.

The basic principle of EGS for exploiting heat stored in rocks at depth is to circulate water through the rock to extract the heat. Hot fluids are extracted through production wells and once the heat has been used directly or for producing electricity, cooled water is reinjected through injection wells.

Typically the rocks that are targeted for geothermal exploitation are not porous and flow paths are located within natural fractures. Since the initial permeability of the rock mass is generally too low for economic heat production, the boreholes have to be stimulated for connecting them to the surrounding environment and for enhancing the water transmissivity of the natural fracture network.

In 1992 and in 1995 two wells (GPK1 and GPK2) were drilled at Soultz to a depth of 3600 m and 3878 m, respectively, to study and exploit the upper part of the geothermal reservoir where temperatures of 160 °C are reached. GPK1 was stimulated in 1993 and GPK2 twice in 1995 and 1996. A circulation test was performed in 1997 between both wells (Baumgärtner *et al*. 1998).

In 1999, GPK2 was deepened and two new deviated wells (GPK3 and GPK4) were drilled in 2002 and 2004, respectively, to depth where rock temperature reaches about 200 °C (Baria *et al*. 2000; Baumgärtner *et al*. 2000). To connect efficiently the boreholes to the fracture network and to improve the global permeability of the reservoir, GPK2 was stimulated in 2000 June/July, GPK3 in 2003 May/June, and GPK4 in 2004 September and again in 2005 February. Presently the reservoir development is completed and exploitation of heat is conducted through a geothermal reservoir whose depth is ranging from 4000 to 5000 m.

In this study we present new results of a time-dependent (4-D) seismic tomography obtained with *P*-waves arrival times for seismic events recorded during the 2000 GPK2 stimulation. During this stimulation more than 11 000 microearthquakes were recorded with the surface network (Cuenot *et al*. 2008). Among them we have selected about 7200 events detected by the surface network which had duration magnitude ranging from –0.9 to 2.5 and were accurately located. As Cuenot *et al*. (2008) did, we performed the 4-D seismic tomography after dividing the main set into chronological subsets to describe temporal changes in the seismic velocity structure during the stimulation. This study differs from theirs in two main points.

First, the subsetting has been performed by taking into account variations of injection parameters (i.e. injection rate, wellhead pressure and downhole pressure). Secondly, the method combines a double difference tomography method (tomoDD, Zhang & Thurber 2003) with an averaging process [weighted average model (WAM), Calò 2009] that corrects for parameter dependence effects. We discuss finally how the precise relocation of seismic events together with the temporal variations of the 3-D *P*-velocity models may shed some light on the non-seismic deformation process induced by the reservoir stimulation.

GEOLOGICAL AND STRUCTURAL SETTING

The Soultz site is located within the Upper Rhine Graben, which is a rift structure that belongs to the West European Rift System (Ziegler 1992; Fig. 1).

The Rhine Graben developed due to extensive E–W strain during the Cenozoic as a result of the Alpine N–S compression. The Upper Rhine Graben extends over 300 km in the N–S to NNE–SSW direction (Fig. 1). Its width is about 30–40 km at the latitude of Soultz. The extension was achieved through a massive fracturing of the upper crust (Brun *et al*. 1991) characterized by large-scale normal faults. The rifting of the Rhine Graben resulted in the thinning of the crust, and therefore in a higher heat flux because of the shallower mantle depth (Clauser *et al*. 2002).

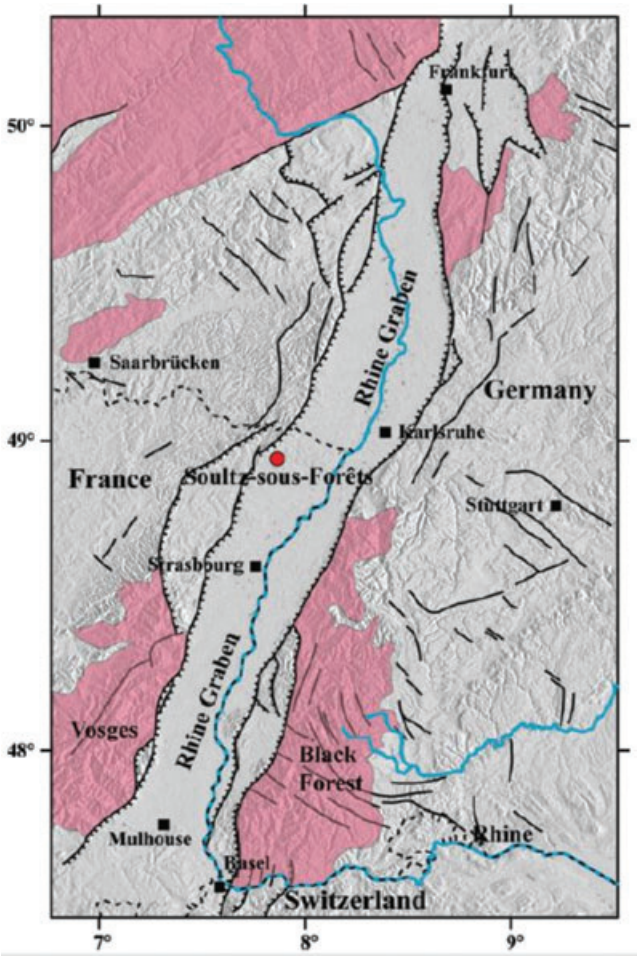

Figure 1. Location of the Soultz-sous-Forets EGS test site in the Rhine Graben. Outcropping crystalline rocks is shown in pink.

The sediment cover is mainly constituted by marine and lacustrine limestone, marls and evaporite, including the petroleum layers of Pechelbronn, which overlay in unconformity the Jurassic limestone and the Trias Formations. These Cenozoic and Mesozoic sediments have been deposited on the palaeozoic basement constituted by a porphyritic monzogranite and a two-mica granite (Genter *et al*. 1999; Stussi *et al*. 2002; Cocherie *et al*. 2004; Hooijkaas *et al*. 2006).

Both Mesozoic rocks and granite are affected by a series of subvertical N–S normal faults dipping westwards or eastwards (Elsass *et al*. 1995). The site of the EGS project is located on a horst structure, named the 'Soultz Horst' after old petroleum explorations (Schnaebele *et al*. 1948). The top of the granitic basement lies at a depth of 1.4 km and constitutes the upper limit of the geothermal reservoir.

The major structural direction estimated in the granite is around N160°E to N–S with high eastward and westward dipping. However, the orientations of fractures observed on cores are rather scattered with various dipping values (Dezayes *et al*. 2010).

HYDRAULIC PARAMETERS, SEISMIC DATA AND SUBSET SELECTION

To improve the connectivity and the permeability of the reservoir, GPK2 was stimulated in 2000 through a high-pressure water injection that lasted 7 d. During this stimulation test, over 23 000 m^3 of fluids were injected (Weidler *et al*. 2002) at three different increasing flow rates (Fig. 2), respectively, 30 L s^{-1} during 24 h (phase 1), 40 L s^{-1} during 27 h (phase2) and 50 L s^{-1} during 90 h (phase 3). The pressure increase, as measured at the wellhead and at the casing-shoe, reached rapidly a maximum of 12–13 MPa during the two first phases of the stimulation. Then it slowly decreased with time. However, during the third phase, when the injection rate reached 50 L s^{-1}, the downhole overpressure first increased to 13 MPa, and then kept increasing up to a maximum value equal to 14.5 MPa just at shut-in. After shut-in (phase 4, Fig. 2), pressure dropped rapidly by 4 MPa and then kept decreasing very slowly (Weidler *et al*. 2002). The continuous pressure increase during the last stimulation phase and the slow pressure decline after shut-in suggest that the stimulated volume behaved like a closed system, that is, without connection to a strongly hydraulically conductive fault system (Dorbath *et al*. 2009).

During and after this stimulation operation, an intense microseismic activity was recorded (Dyer 2001; Cuenot *et al*. 2008). The seismic network used in this work consisted of 14 surface stations and three downhole stations (Fig. 3a). The surface network was installed by EOST, University of Strasbourg, and consisted of different types of seismological stations (eight 1 Hz single vertical seismometers and six 1-Hz three-components seismometers, Cuenot *et al*. 2008). The downhole sensors (four components accelerometers) were installed in wells 4550, 4601 and OPS4 at a depth of about 1.5 km (Fig. 3b), which corresponds to the top of granite. Surface acquisition was conducted with a sampling rate of 180 sps per channel while the downhole network operated at 2000 sps per channel. About 11 000 induced events were detected by the surface network and about 14 000 with the downhole stations. Arrival times for *P* and *S* waves were manually picked with errors estimated to be smaller than 0.01 s, given the sampling rate and the clear onset of *P* and *S* waves. We decided to use the set of 7215

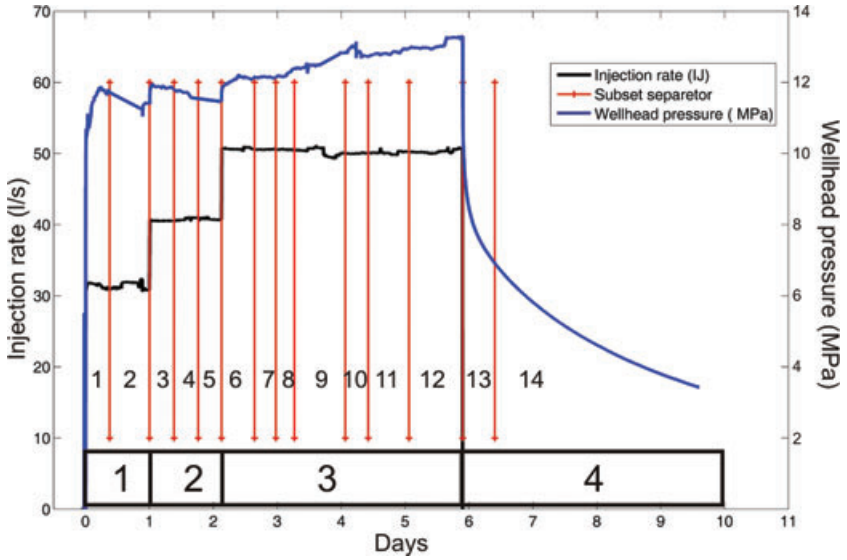

Figure 2. Injection rate (black line) and overpressure (blue line) measured at GPK2 wellhead. The four main phases of the stimulation test are shown in black and the subsetting into fourteen sets for the 4-D tomography is shown in red.

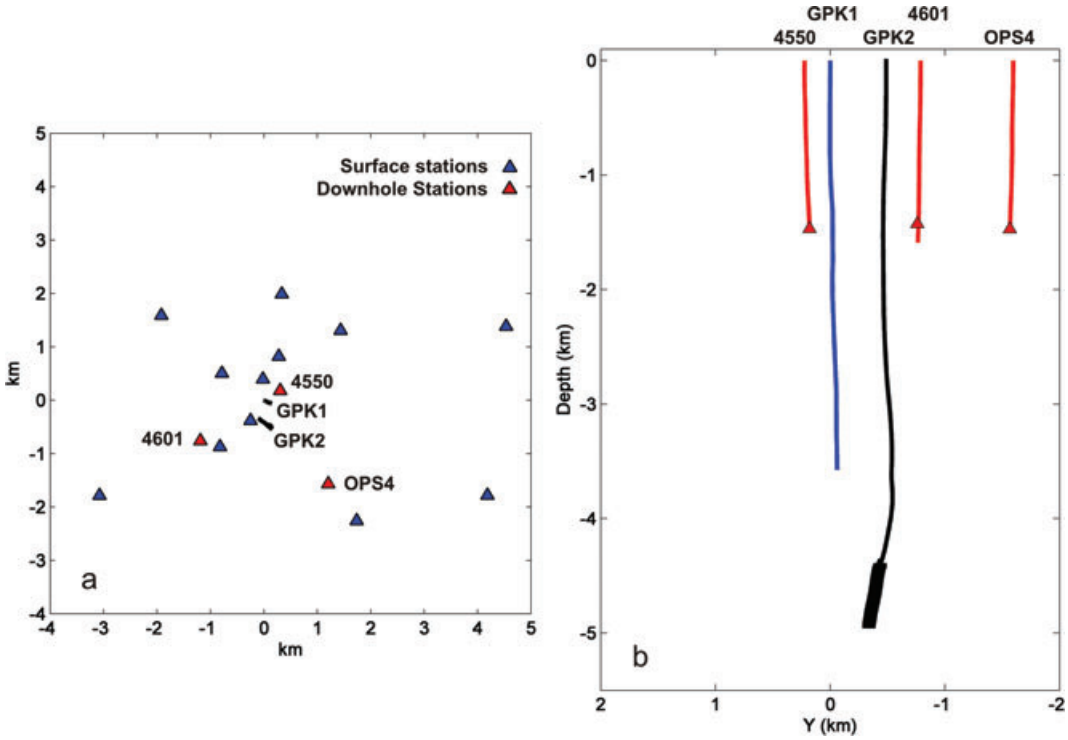

Figure 3. Downhole and surface seismological stations installed during the 2000 stimulation test. (a) Plane view of the configuration for both networks. The type of sensor at each station is indicated by different colour and the wellheads of GPK1 and GPK2 wells are plotted on the map. (b) Vertical view of the borehole geometry. The thick part of GPK2 corresponds to the open-hole section of the well.

events that Cuenot *et al*. (2008) defined for conducting their seismic tomography. These events have been located using at least eight *P*- and three *S*-arrival times. On average most events have been located using 12 *P* and five *S* phases. The initial 1-D horizontally layered velocity model used for locating events was derived from sonic logs and calibration shots performed in the GPK1 well (Beauce *et al*. 1991). To improve the preliminary hypocentre locations Cuenot *et al*. (2008) refined the velocity model and applied station corrections. Both were iteratively calculated by minimizing residual errors at the stations. Then, the rms after the relocation procedure resulted in a maximum value of 0.02 s for all 7215 events (Cuenot *et al*. 2008).

Events duration magnitudes range from –0.9 to 2.5 for the recording period (June 30–July 11). Hypocentres are located in a limited region around GPK2 at a depth ranging from 4000 m to 5000 m. The shape of the seismic cluster is elongated in the N 145°E direction and extends up to 1 km away from the stimulated well.

Cuenot *et al*. (2008) divided the main database into 13 chronological sets of 500 events each plus one set of about 700 events for investigating the temporal evolution of the velocity structures.

Table 1. Time period, number of events, absolute data (*P* and *S*) and differential data (*P* and *S*) for the 14 sets.

Subset	Time period	*N* events	Abs. *P* phases	Abs. *S* phases	Diff. *P* data	Diff. *S* data
1	06/30 h 19:15 07/01 h 03:40	300	3131	1162	32839	9167
2	07/01 h 03:41 07/01 h 18:39	600	6443	1874	65316	15351
3	07/01 h 18:39 07/02 h 03:50	630	5807	2105	59163	17907
4	07/02 h 03:50 07/02 h 12:57	490	6807	1782	43582	14809
5	07/02 h 12:58 07/02 h 21:39	240	2246	674	23429	6324
6	07/02 h 21:46 07/03 h 10:04	490	4382	900	44049	6402
7	07/03 h 10:04 07/03 h 18:06	550	5836	2040	59341	17470
8	07/03 h 18:07 07/04 h 10:25	540	5745	2068	58460	17391
9	07/04 h 10:32 07/04 h 20:11	780	7192	2545	71515	22830
10	07/04 h 20:12 07/05 h 04:45	480	4493	1344	47121	12977
11	07/05 h 04:47 07/05 h 20:06	600	6701	2469	63488	20140
12	07/05 h 20:07 07/06 h 16:10	780	8659	3440	81361	20140
13	07/06 h 16:10 07/07 h 04:18	285	3213	1328	28826	11296
14	07/07 h 04:32 07/11 h 00:55	450	5098	1951	43835	13977

We decided here to apply the tomographic method to 14 not-equally populated sets to fit better with characteristics of the hydraulic stimulation (Fig. 2). Indeed, it may be assumed that strong perturbations in the reservoir are more likely to occur during injection phase transitions rather than during uniform injection pressure periods. Hence subsetting the data according to the injection characteristics is more likely to provide a pertinent description of the seismic velocity temporal evolution.

The seismic data sets covering periods 1, 2, 3, 5, 6, 12 and 13 have been chosen to fit the highest variations of the injection flow rate, while the other ones (4, 7, 8, 9, 10, 11 and 14) have been introduced to observe the evolution of the velocity model when no change in injection rate occurs. Table 1 reports the time period, the number of events and the number of phases (*P* and *S*) for each set. The smallest set contains 240 events to maintain ray coverage dense enough to get an acceptable reliability for the recovered velocity models. The largest sets include 780 events.

METHOD

For each subset, we first ran the tomoDD code (Zhang & Thurber 2003) to solve the V_P and V_S structures and hypocentral locations. Then the post-processing WAM method was run to increase the volume of investigation and to improve the reliability of the velocity models (Calò 2009).

The double-difference tomography code (Zhang & Thurber 2003) has been developed to solve event locations and velocity structure simultaneously by using both absolute and differential traveltime data. This process overcomes the limitation of the double-difference location method (Waldhauser & Ellsworth 2000) by taking into account explicitly the path anomaly biases between pairs of events. In theory, double-difference tomography has the ability to relocate accurately large numbers of earthquakes both in absolute and relative locations as well as to characterize more precisely the local velocity structure. Many areas have been studied by using this technique at local and regional scale (Zhang & Thurber 2003; Thurber *et al*. 2003; Shelly *et al*. 2006; Dorbath *et al*. 2008), allowing a detailed description of the V_P and V_S velocity structures where the seismicity is highly clustered.

The observed differential arrival times can be calculated from both waveform cross-correlation techniques for similar waveforms and absolute catalogue arrival times. In our work we calculated differential times from the absolute arrival times catalogue only.

The initial horizontal nodes spacing for the DD tomography is 250 m in the *X* and *Y* directions near the centre of the grid, where most hypocentres lie and where a maximal resolution is required (Fig. 4a). This part of the grid is 3.5 km × 3.5 km in both the *X* and *Y* directions. Near the boundaries of the mesh, where seismicity is sparser, gridpoints are spaced every 500–1000 m. Dimension of the whole grid (excluding external nodes) is then 6 km × 6 km (Fig. 4a). To be consistent with previous studies, we chose GPK1 wellhead (48.93537 N, 7.86535 E, altitude 153 m) as the geographical origin for the gridpoints. Note that there is no symmetry of the grid relatively to this origin. In depth, we positioned the grid layers each 0.4 km between 0.0 km and 1.6 km. This range corresponds to the main sedimentary layers. At a depth of 1.6 km, the top of the granite massif is reached. Below this depth the vertical spacing is fixed to 0.5 km (black thick dashes, Fig. 4b).

However, in tomoDD (as well as in whatever tomographic inversion code) the initial parameters that are imposed for obtaining the 3-D velocity models (e.g. initial model velocity values, model

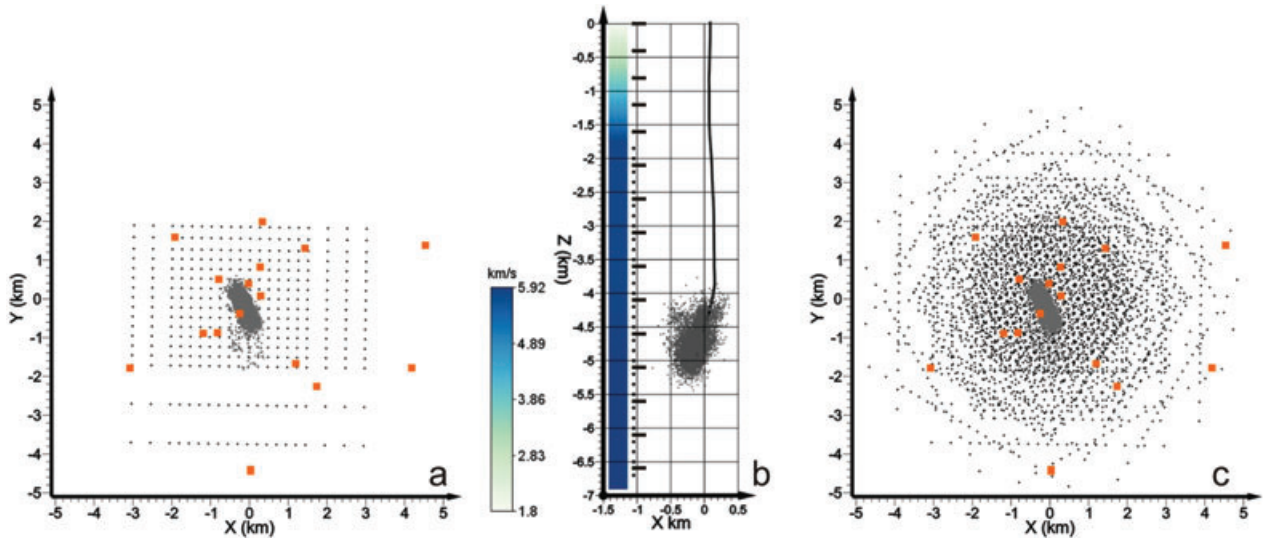

Figure 4. (a) Map of seismicity (grey dots), seismic stations (orange squares), and initial inversion grid (black dots) used to perform a standard double-difference tomography. (b) Initial 1-D velocity model and projection of GPK2 and seismicity. The bold lines in the 1-D velocity model are the depths sampled by the initial inversion grid of Fig. 4(a). The black dots together with the bold lines are the depths of the 1-D velocity model sampled with the WAM method. (c) Nodes of the 15 inversion grids used to estimate the velocities with the WAM method.

parametrization and data selections) may strongly affect the results. We applied the WAM method (Calò 2009) to overcome this potential bias. The WAM method is based on sampling models compatible with data sets using different input parameters and then synthesizing results in a WAM. The WAM method is a post-processing technique that may be used with any tomographic inversion code (see Appendix A).

With the WAM method the final velocity values are the weighted mean of velocities obtained after performing numerous inversions. In this study we used the derivative weight sum (DWS, Toomey & Foulger 1989) as the weighting factor, for it is directly related to the experimental information used to determine the velocity during the ith inversion.

To construct the WAM we performed, for each set of data, 12 inversions in which the initial inversion grid was rotated by 30° steps and three inversions that sampled the 1-D initial model at different depths. Therefore the number of models with different gridpoint positions carried out for constructing the WAM is 15. Fig. 4(c) shows the horizontal density sampling of the investigated volume with the WAM method while in Fig. 4(b) black points (together with the black thick dashes) represent the sampled depths of the 1-D initial velocity model.

In the WAM method, all possible input parameters are varied for obtaining a statistically independent solution. In tomoDD the absolute and differential data are weighted at each iteration, then the weighting scheme should be considered as another input parameter that has to be optimized. Several tests have been performed by varying the weighting scheme of the data. Since the seismic cluster is very concentrated, very similar results are obtained whatever the weighting data scheme. Hence, we chose not to integrate further inversions in the WAM, for they did not provide new information even though the weighting scheme of the data was varied significantly.

To assess the reliability of the method (tomoDD plus WAM) and the resolution power of the data we performed some synthetic tests (see Appendix A) and reported the weighted standard deviations (WSTD) for the 14 velocity models forming our time-lapse tomography (see Appendix B).

TEMPORAL EVOLUTION OF THE *P*-WAVE VELOCITY FIELD

14 WAMs have been computed from the 14 sets reported in Table 1 to observe the temporal evolution of V_P field in the geothermal reservoir. The sets have been selected according to the four main stimulation phases described earlier. The results are presented on three figures, which are discussed simultaneously hereafter.

The V_P models are shown in Fig. 5 (horizontal sections at 4.6 km depth) and Fig. 6 (vertical sections striking about N150°E along the A–B line in Fig. 5). The blue-purple line in Fig. 5 is the projection of GPK2, while in Fig. 6 are reported the projections of both GPK2 and GPK1. The thick part of GPK2 trajectory corresponds to the open-hole section of the well. It is located within the 4.4 to 5 km depth interval.

For all the sets, only the well resolved part of the model (DWS > 10) is displayed. For each set we report the projection of events used to obtain the model. Black contours correspond to velocity isovalues, respectively, equal to 5.4 km s^{-1}, 5.7 km s^{-1}, 5.85 km s^{-1} and 6.05 km s^{-1}.

The corresponding V_P WSTD are reported in Appendix B to assess the reliability of observed V_P spatial variations. The standard deviations are smaller than 0.025 km s^{-1} for most of the 14 sets. They reach 0.05 km s^{-1} in few areas and this only for some of the sets. These values are significantly lower than the amplitude of the velocity variation observed in the area, and even considering an error bar of 2σ (∼95 per cent confidence interval), the reliability of the anomalies remains very high. Furthermore the absence of spatial correlation between the highest WSTD and the velocity anomalies ensures the low dependence of the velocity models on the initial parameters and therefore supports the reliability of the results.

The V_P value in the 1-D reference velocity model at 4.6 km depth is 5.85 km s^{-1}. Thereafter we discuss the seismic velocity anomalies with values at least equal to ±0.15 km s^{-1} from the initial 1-D model and WSTD < 0.03 km s^{-1}, and we consider as 'strong' anomalies regions with values at least equal to ±0.45 km s^{-1} from the starting model.

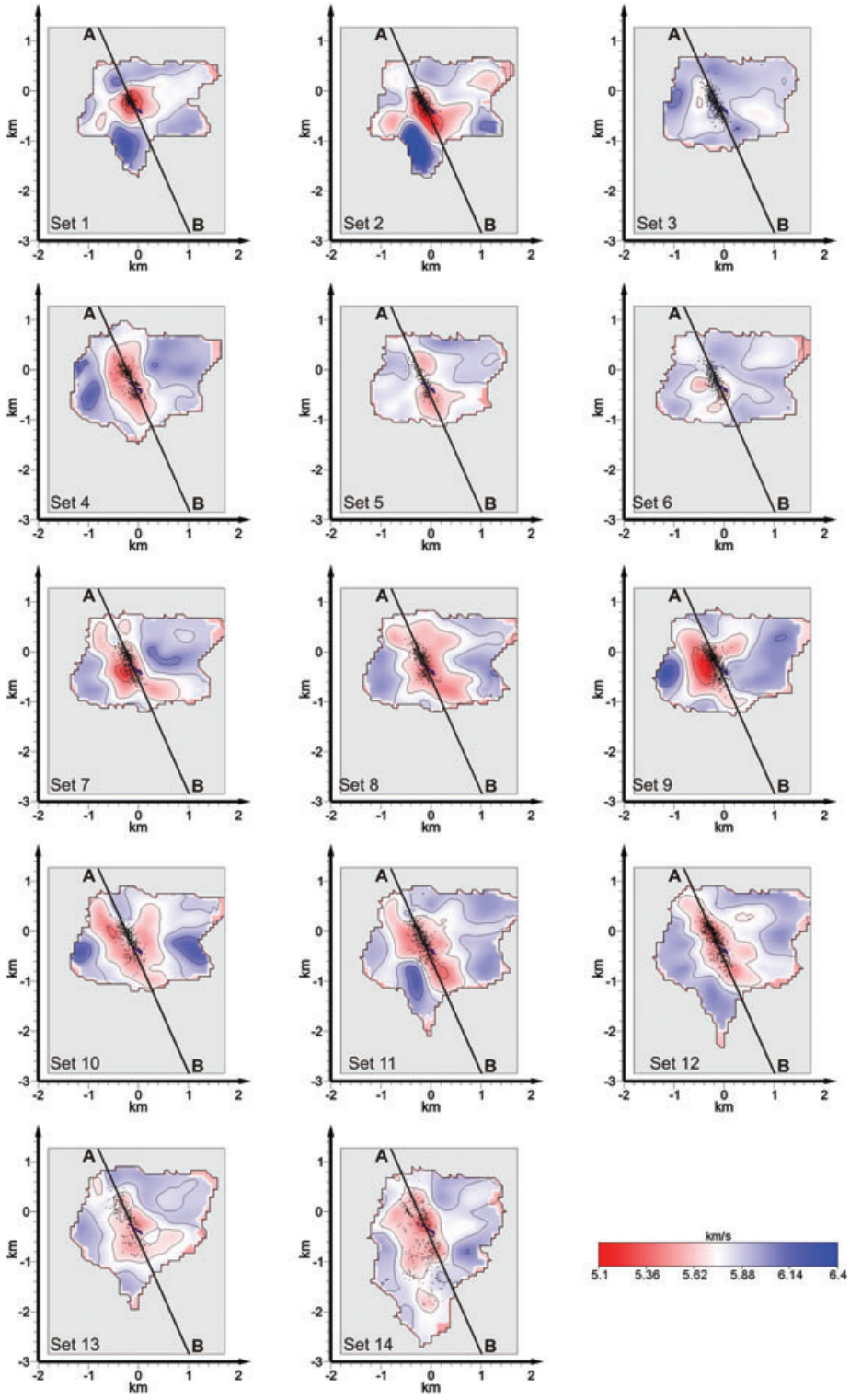

Figure 5. Evolution of the *P*-wave seismic velocity at 4.6 km depth during the 2000 stimulation test. Images are in chronological order from set 1 to set 14. The black dots are the projections of the events used to obtain the V_P models. Profiles A–B are the traces of the vertical sections reported in Fig. 6.

Fig. 7 shows the final epicentre locations for the 14 sets. The size of the circle of each event is proportional to its magnitude.

The initial location of events used to perform the time-domain tomography comes from an accurate analysis discussed by Cuenot *et al*. (2008). They estimated the mathematical error on their event locations to be 100 m for the epicentre positions and 80 m for the depths. The mean rms of the located events was 0.017 s.

The tomoDD code provides simultaneously event locations and velocity structure. The WAM method combines, beside the velocity

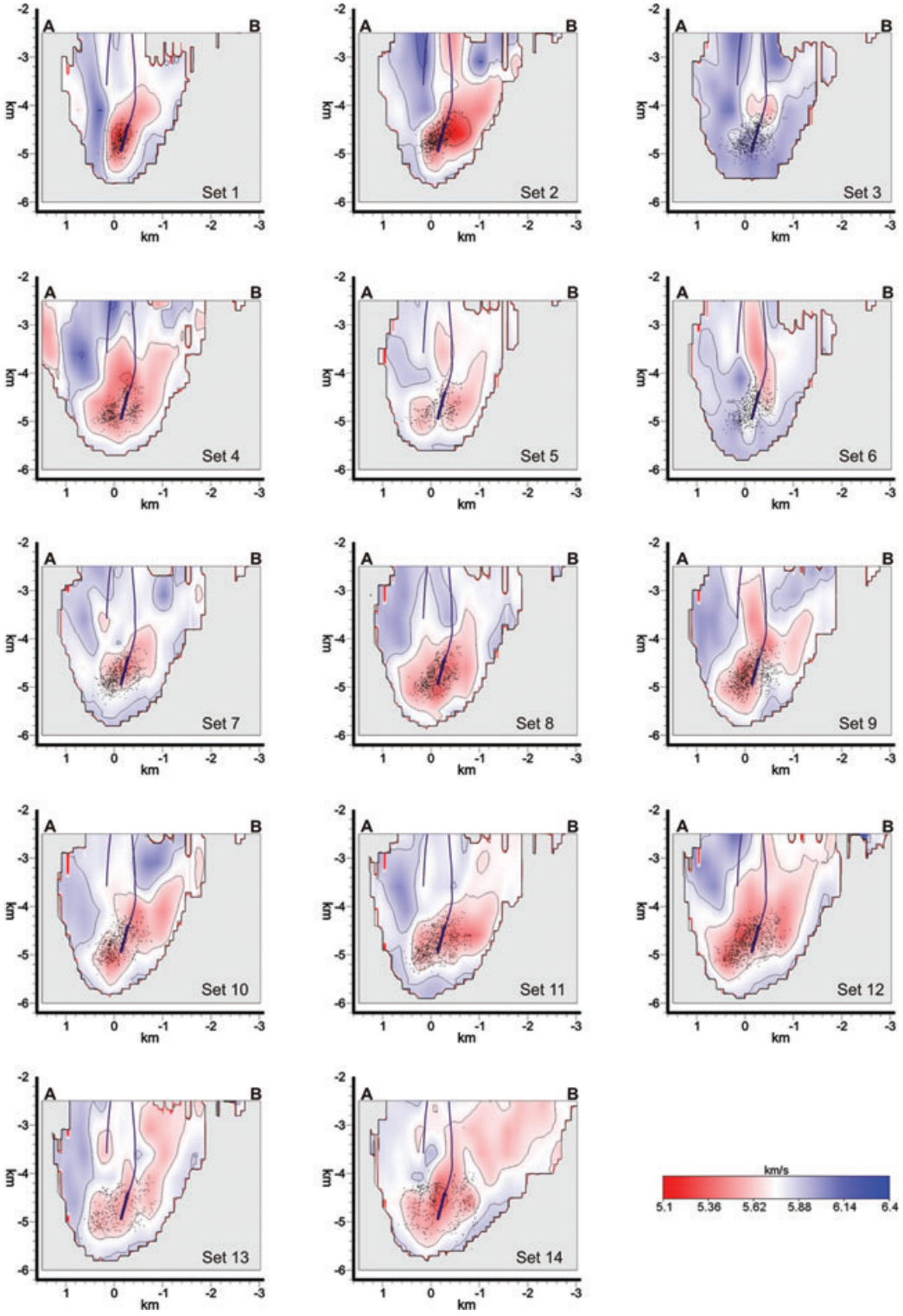

Figure 6. Vertical sections of the V_P models along traces A–B reported in Fig. 5. The black dots are the projections of the events used to obtain the V_P models. Blue lines are the projections of GPK1 and GPK2. The thick part of the borehole trajectory corresponds to the open-hole section of GPK2 well.

models, the final hypocentre locations resulting from each inversion, using the rms of the events as weighting factor. We estimate that, with the applied methods (tomoDD plus WAM), the mathematical uncertainty on the epicentre positions is less than 30 m while it is about 50 m for depths. The mean rms is 0.011 s. It is worth noting that the mean rms corresponds to the mean picking errors estimated for the *P* and *S* phases (Cuenot *et al*. 2008). The calculated mean rms suggests that a minimum misfit between the hypocentres model and the space of the possible models has been reached. Lower values of the mean rms would have been smaller than the estimated picking errors and would not have provided further improvements on the accuracy of hypocentre locations.

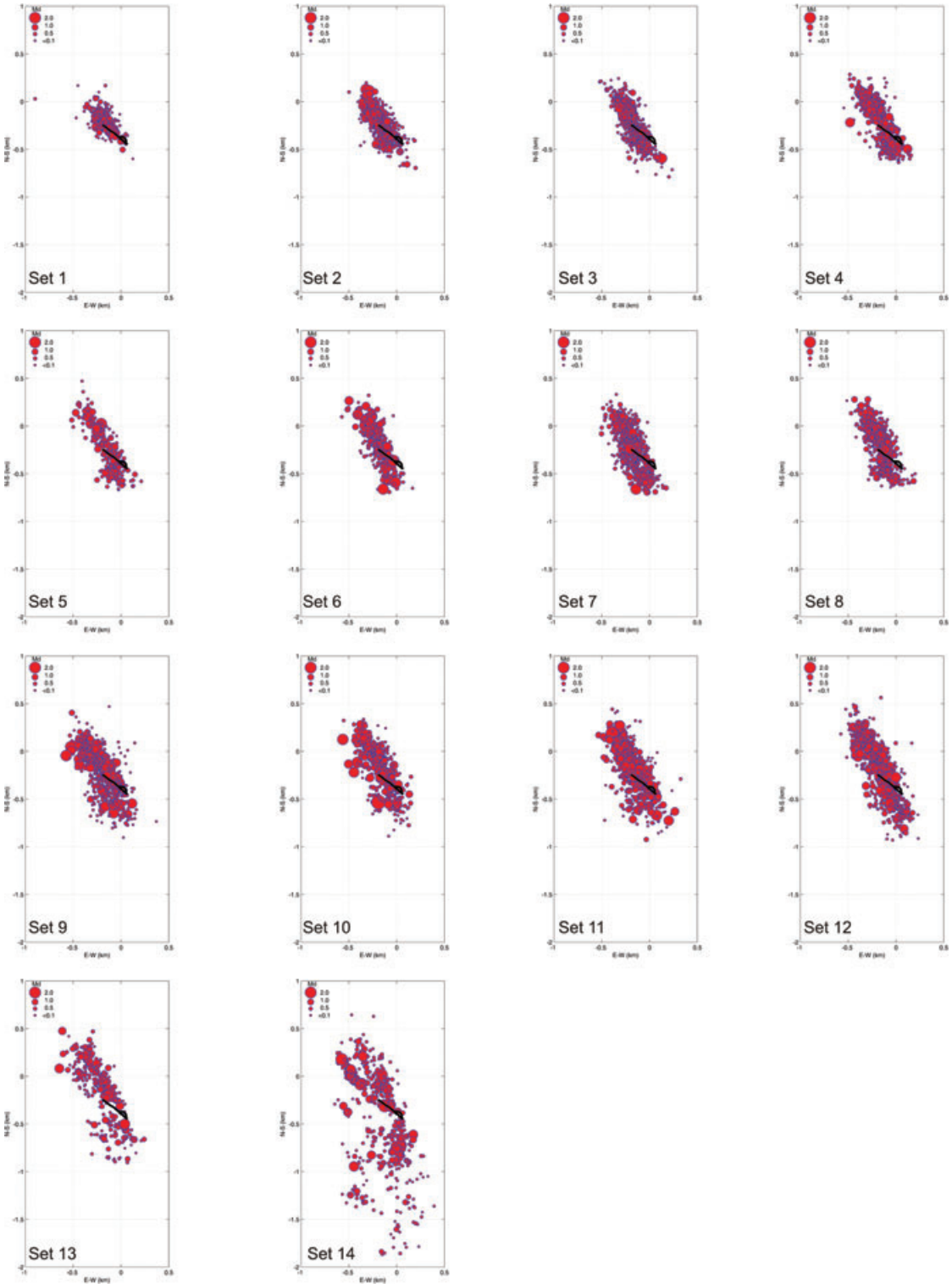

Figure 7. Evolution of the microseismic cloud. Each picture shows, in chronological order, the final event positions after the computation of the local tomography. The radius of each circle is proportional to the magnitude and the projection of the injection well is indicated as a black line.

PHASE 1, SETS 1–2

Set 1 shows the mean state of the reservoir during the first 8 h of the stimulation when the injection rate was 30 L s^{-1} (Fig. 3). At a depth of 4.6 km a strong low V_P area ($5.25 < V_P < 5.7$ km s^{-1}) with circular shape is clearly visible around GPK2 (Fig. 5.1). The projected seismicity is centred around GPK2 and into the low V_P area as well. The close match between the position of the well, the seismicity distribution and the low V_P anomaly is even clearer on the corresponding vertical section (Fig. 6.1). The strong low V_P ($V_P < 5.4$ km s^{-1}) is roughly located around the open-hole section of GPK2. Thus, at the beginning of the stimulation, the *P*-velocity

perturbation is strictly localized around the well, within 250 m away from the well.

Fig. 7.1 images the relocated events of set 1 as a compact cloud slightly elongated in the N150°E direction, without any visible organization along any minor structures.

Set 2 includes all events that occurred during the next 16 h, until the end of phase 1 (Fig. 2). The low V_P area ($5.1 < V_P < 5.7$ km s^{-1}) widens towards the SE (Fig. 5.2) and encloses almost all associated events. Nevertheless, the extension of the strong low V_P anomaly is much larger than the migration of seismicity. The vertical cross-section (Fig. 6.2) clearly shows the extension of the V_P anomaly towards the southeastern part of the stimulated reservoir, while the seismicity remains to the NW of GPK2 open-hole section. The maximum extension of the seismically active area increased from 0.4 km (set 1) up to about 0.7 km within a few hours (Fig. 7.2).

PHASE 2, SETS 3–5

Set 3 includes events that occurred during the initial 9 h of the second injection phase, when injection rate was 40 L s^{-1}. In this set the strong anomaly at depth disappears. Fig. 5.3 shows the presence of a very weak low V_P anomaly ($V_P \approx 5.7$ km s^{-1}) located west of the seismic cloud. The spatial correlation between location of events and the zone that shows a drop in seismic velocity is no more notable. Also, seismicity is observed in the whole low-velocity area of the previous set, (set 2). A low V_P anomaly ($5.5 < V_P < 5.7$ km s^{-1}) remains at a depth of about 3.8–4.2 km, just above the seismic cloud (Fig. 6.3). That part of the model where this low V_P anomaly is located matches the volume of the reservoir stimulated during the GPK2 injection test in 1997, before its deepening (Baumgärtner *et al*. 1998). Then the velocity model varies at all depths within the reservoir after the injection rate increase. Furthermore, the spatial distribution of the seismicity does not change significantly (Fig. 7.3). The area affected by events is still oriented N150°E and its length increases slowly, reaching a maximum value equal to about 1 km.

In set 4, a low V_P anomaly ($5.45 < V_P < 5.7$ km s^{-1}) elongated in the N150°E direction is identified (Fig. 5.4). It is larger although less marked than in the previous set 2. Here, the seismic cloud is again well centred on the V_P anomalous region. The larger dimension of this anomaly is also clearly visible on the vertical cross-section (Fig. 6.4). Its vertical extension is estimated to be about 2 km (by taking as reference the isocontour 5.7 km s^{-1}) while the horizontal one (along the NNW–SSE direction) reaches at least 1.8 km. Fig. 7.4 shows that the area involved by the seismicity does not change significantly.

Set 5 includes events that occurred up to the end of phase 2. This set depicts a scenario similar to the previous one although slightly smoothed and less contrasted. We observe the same region affected by the low anomaly, but it is more diffuse ($5.5 < V_P < 5.7$ km s^{-1}) (Figs 5.5 and 6.5). The observed low-velocity anomaly seems to be disappearing slowly, contrarily to what was observed before the end of phase 1 (set 2). Fig. 7.5 displays a seismic cloud similar to that of set 4.

PHASE 3, SETS 6–12

Set 6 shows the mean state of the reservoir during the first 12 h of phase 3, when injection rate is equal to 50 L s^{-1} (Fig. 2). The low V_P anomaly ($V_P \approx 5.7$ km s^{-1}) keeps decreasing in size and amplitude, and it is not spatially correlated with the seismic cloud (Fig. 5.6). The vertical section of Fig. 6.6 shows the quasi-total absence of V_P anomalies at the depth of stimulation (4.4–5 km) while a slight anomaly ($5.55 < V_P < 5.7$ km s^{-1}) is observed above the seismic cloud, between depths 2.6 km and 4.7 km. The shape and size of the seismicity does not vary significantly (Fig. 7.6).

This set may be compared with set 3, for both are representative of the reservoir immediately after a strong injection rate increase. Both V_P models show similar features with low V_P above the seismic clouds and no spatial correlation between V_P perturbations and seismic cloud. However, they differ in the way they develop: the increase of P velocity is sudden between sets 2 and 3 but progressive between sets 5 and 6. The other sets discussed until now show a large spatial consistency between low V_P anomalies and seismic clusters. Furthermore, the shape of low V_P anomalies are always N150°E oriented and much larger than the region where seismicity occurred.

Set 7 includes events that occurred during the next 8 h, when GPK2 wellhead pressure remained constant at 12.1 MPa (Fig. 2). The large low V_P anomaly ($5.5 < V_P < 5.7$ km s^{-1}) (Fig. 5.7) starts enclosing completely the seismic cloud that extends into regions that were not seismic, towards the north and the south. A small strong low V_P area is partially located west of GPK2 and of the seismic cluster. Fig. 6.7 shows that the main low V_P area is located between 3.8 km and 5.2 km depth. Furthermore a small low V_P anomaly ($5.6 < V_P < 5.7$ km s^{-1}) is present near the bottom of GPK1. This well was stimulated at this depth in 1993 through high-pressure fluids injection also. Compared with the previous set, the seismicity (Fig. 7.7) does not extend any longer along the main strike of the seismicity cloud. On the contrary it starts extending in the E–W direction.

Set 8 includes events that occurred when GPK2 wellhead pressure increased slowly from 12.1 MPa to 12.4 MPa, although the injection rate was constant at 50 L s^{-1}. Fig. 5.8 shows a low V_P anomaly ($5.4 < V_P < 5.7$ km s^{-1}) that keeps thickening, especially at the N–NW and to the S–SE of the cluster, in regions without seismic activity. Fig. 6.8 shows the large area involved in this V_P anomaly, affecting the reservoir from 3.8 km to 5.5 km depth. The shape of the seismic cluster does not change (Fig. 7.8).

During set 9, the wellhead pressure increases constantly from 12.4 MPa to 12.8 Mpa. On this set (Fig. 5.9), a strong low V_P anomaly ($5.1 < V_P < 5.4$ km s^{-1}), larger than on set 7, develops west of the seismic cloud. However, nearly all the seismicity is enclosed within the low V_P area. The low velocities extend up to 2.8 km (Fig. 6.9). The seismic cloud (Fig. 7.9) extends again, reaching a maximum length of 1 km.

Set 10 contains events recorded during a small drop (from 13 MPa to 12.65 MPa) in GPK2 wellhead pressure (Fig. 2). The strong low V_P area observed in set 9 disappears; however the larger and weaker one is still present, with an extension towards the north similar to what was observed in sets 8 and 9 (Fig. 5.10). The low V_P region extends from 3.6 km to 5.6 km depth (Fig. 6.10), while the seismic cloud slightly extends towards SE (Fig. 7.10).

Sets 11 and 12 include events that occurred up to the end of phase 3. During this period the wellhead pressure increased constantly from 12.65 MPa up to 13.3 MPa (Fig. 2). The two sets (Fig. 5.11 and 5.12) are quite similar. The seismicity is centred into the low V_P anomaly ($5.4 < V_P < 5.7$ km s^{-1}), which is still much larger than the size of the cluster and is elongated along the NW–SE direction. The low V_P anomalies are located roughly at the same depth (Fig. 6.11 and 6.12), although an extension to shallower depth is observed on set 12. Figs 7.11 and 7.12 show dense seismic clouds growing in

the SE direction, with a maximum elongation equal to 1.2 km and 1.3 km for set 11 and 12, respectively.

PHASE 4, SETS 13–14

Set 13 includes events recorded during the 12 h that followed shut in. The low V_P anomaly ($5.5 < V_P < 5.7$ km s^{-1}) widens in the E–W direction although keeping its main elongation in the NW–SE direction. A low V_P area encloses completely the seismicity around GPK2 (Fig. 6.13), while a low V_P anomaly is also observable around GPK1. On this section the seismicity is located away from GPK2, highlighting a region near the well with a gap of seismic events. The seismic cloud is well defined on the eastern side while it is more diffuse on the western one (Fig. 7.13).

Set 14 includes all the remaining events that occurred after shut-in, during a period that lasted about 4.5 d (Fig. 2). Fig. 5.14 shows that the NNW–SSE low V_P area ($5.3 < V_P < 5.7$ km s^{-1}) is still present. It is worth noting that the lower V_P anomaly ($V_P <$ 5.4 km s^{-1}) is located around GPK2, exactly at the same place as the first anomaly for set 1 (Fig. 5.1). The vertical section (Fig. 6.14) shows a low V_P area around GPK2 extending from 2.5 km to 5.6 km. The shallowest part of the V_P anomaly is located in the southern part of the investigated volume. A small low V_P anomaly is still observable close to the bottom of GPK1. The depth of seismicity is ranging from 4.3 km to 5.4 km. It extends much farther towards the south (Fig. 7.14) in a large area extending for 2.3 km along the NNW–SSE direction. It is about 1 km wide. The seismic cloud takes a Y shape in its northern part outlining at least two main internally active structures. The western branch of this structure seems to be characterized by a larger and better organized seismicity. The southern part of the cloud, wide and rather sparse, is new.

DISCUSSION

This 4-D tomography has led to identifying temporal changes of the V_P velocity field during and after the injection test. We may shortly summarize the main observations as follows:

(1) All the sets, except set 3 and set 6, present grossly similar features: a low-velocity anomaly located mainly around the zone where microseismic activity develops, but larger than this seismic cloud. Immediately after the very beginning of injection (set 1), the velocity anomaly is circular in shape on a map view. It gets elongated in the N145– N150°E direction during set 2, and this direction does not change thereafter.

(2) Sets 3 and 6, represent the reservoir within the few hours that follow an injection rate increase by 10 L s^{-1} and show a return of the seismic velocity field to its initial value within the injection region.

Our results concerning the evolution of the relocated seismic cloud during the stimulation experiment do not differ from those extensively discussed by Cuenot *et al*. (2008). Starting from set 2, the seismicity strikes N145° to N150°E, which is 20–25° off the maximum horizontal principal stress (σ_H) direction as determined from borehole failure mechanisms (Cornet *et al*. 2007; Valley & Evans 2007) but only 5° to 10° from the σ_H direction derived from focal mechanisms inversion (Dorbath *et al*. 2010). The maximum length of the cluster increases from 0.3 km (set 1) up to about 1.0 km (set 3), developing towards the N150°E direction. This extension does not increase until set 9, when the area involved by the seismicity enlarges and reaches its maximum elongation of about 1.3 km

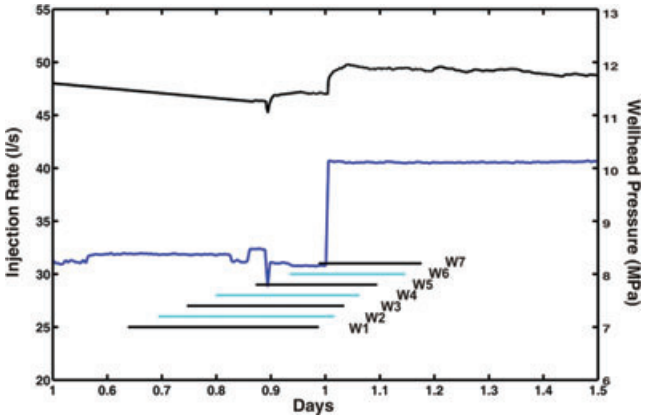

Figure 8. Zoom on the injection rate (black line) and overpressure (blue line) measured at the wellhead of GPK2 between phases 1 and 2 when the injected rate increases from 30 to 40 L s^{-1}. The black and grey lines show the shifting of the temporal windows used to obtain the 4-D tomography. Each window contains 300 events and each shift involves 50 earthquakes.

in set 12. By contrast, for both sets 13 and 14, the seismic cloud gets structured differently. This result was not clear in Cuenot *et al*. (2008) and is supported by the more precise relocation obtained using double-difference method. In set 13, we observe a narrower cluster, more concentrated in its eastern part. In set 14, many events are clustered along at least two preferential directions that are possible expressions of large pre-existing internal structures striking NW–SE to NNW–SSE. This is supported also by the observation that the westernmost alignment is marked by a concentration of larger magnitude events. South of GPK2, the seismicity is sparser but extends significantly towards the south.

It is not straightforward to compare our tomography results to those obtained by Cuenot *et al*. (2008), as the chronological division is quite different. Over all, the amplitude of the low-velocity perturbation and their extension are about the same, although they are much more constrained and delimited in our study.

The most intriguing result of this study is the increase of *P*-wave velocity, back to the initial value, observed for the two sets that correspond to periods just after injection rate increases. It is sudden when the rate increases from 30 to 40 L s^{-1} but more progressive when the rate increases from 40 to 50 L s^{-1}. There was absolutely no indication of such a result in Cuenot *et al*. (2008), because of the inadequate subsetting of the seismicity. Therefore, we decided to assess the validity of our result through a complementary test.

We performed a new detailed 4-D seismic tomography for the transition between phase 1 and phase 2 by using different temporal windows. We selected a set of 600 seismic events recorded during 13 h; 300 of which occurred before the end of phase 1 (when the flow rate was 30 L s^{-1}) and 300 of which occurred at the beginning of phase 2 (when the flow rate was 40 L s^{-1}). We obtained seven subsets shifting each window of 300 events by 50 earthquakes (Fig. 8). The sequence illustrates in detail the evolution of the V_P perturbation during the change of flow rate, between set 2 and set 3. Results presented on Figs 9 and 10 are very clear. While integrating more and more events that occurred during phase 2, we observe a gradual attenuation of the V_P anomaly at the 4.6 km depth and its progressive migration towards shallower depths.

The factors affecting seismic velocity include lithology, porosity, confining pressure, pore pressure, saturation or phase transitions (liquid-vapour) and temperature (Nur 1987). In the Soultz case, the lithology is uniform (granite) and no vapour was present within the

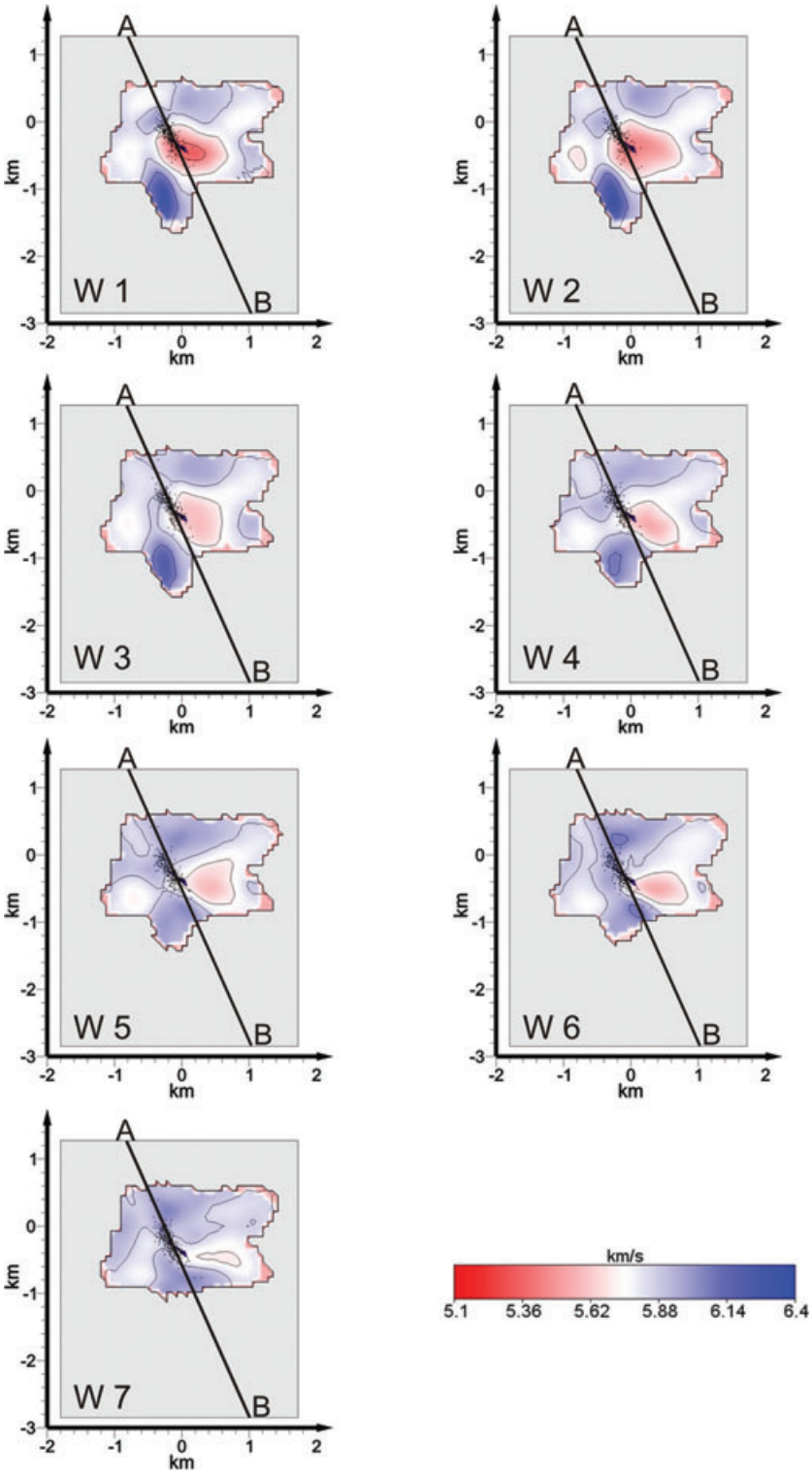

Figure 9. Evolution of the *P*-wave seismic velocity at 4.6 km depth during the transition between phase 1 and 2. Images are in chronological order from window 1 to window 7. Black dots are the projections of events used to obtain the V_P models. Profiles A–B are the traces of the vertical sections reported in Fig. 10.

granite before stimulation, therefore the velocity variations may be attributed only to changes in fluid content or to changes in temperature. However, the decrease in temperature that may have resulted from the injection of cold water in this hot formation would have resulted in an increase in velocity, which is opposite to observation. Hence only changes in liquid content associated to variations in effective stresses are considered to be responsible for the decrease in *P*-wave velocity.

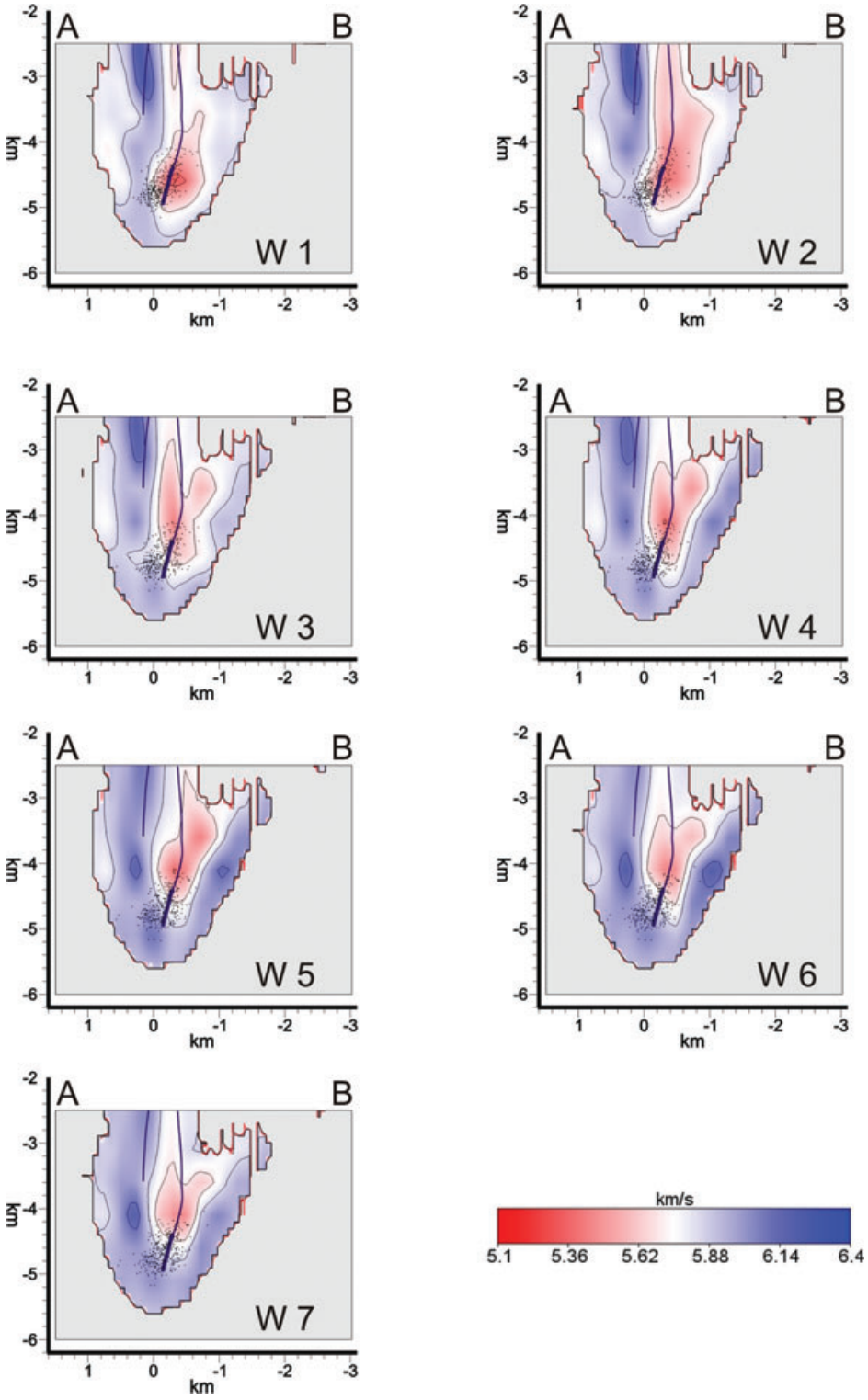

Figure 10. Vertical sections of the V_P models along traces A–B reported in Fig. 9. Black dots are the projections of events used to obtain the V_P models. Blue lines are the projections of GPK1 and GPK2. The thick part of the borehole trajectory corresponds to the open-hole section of the well.

Two phenomena are observed:

(1) A decrease in velocity roughly surrounding the location of induced microseismic activity during most of the injection duration, but with a size larger than that of the seismic cloud. The decrease in *P*-wave velocity remains smaller than 10 per cent of original values.

(2) A sudden return to original V_P values, after changes in flow rate and therefore after a localized change in pore pressure.

We address first the decrease in velocity observed during most of the fluid injection. It has long been known that *P*- and *S*-wave velocities in granite are strongly dependent on the effective stress field applied on the rock (Nur & Simmons 1969; Hadley 1976).

For example, Lockner *et al*. (1977) showed that up to 30 per cent decrease in V_P values occurred in Westerley granite samples loaded up to failure, while Stanchits *et al*. (2003) demonstrated the role of pore fluid pressure variations caused by loading and the correlative dilatancy effects. The role of hydrostatic stress variations has also been demonstrated by Meglis *et al*. (1996) or Reuschlé *et al*. (2006) who showed that variations of effective hydrostatic stress of the order of a few tens of MPa may result in velocity variations equal to many tens of kilometres per second.

We propose that the increase in pore pressure dp close to the injection well resulted in an increase in the effective Coulomb shear stress ($\tau - \mu[\sigma_n - (p + \mathrm{d}p)]$, where μ is the friction coefficient and τ is the shear stress component and σ_n the normal stress component in the plane of interest) so that a shear zone with associated dilatancy has developed. This localized dilatant zone resulted in an increase in fluid diffusivity which favoured fluid diffusion locally and helped further propagate the shear zone within the rock mass. This is consistent with the initial roughly symmetrical shape of the V_P anomaly and its progressive extension in the N150°E direction (recall the maximum horizontal principal stress is close to N170°E). The extension of the anomaly in a domain larger than that of the seismic cloud may be interpreted as a change in effective stress field caused by the development of the dilatant zone. Such a stress perturbation has been modelled as an Eshelby inclusion (Eschelby 1957), for a somewhat similar induced seismicity example at Le Mayet de Montagne, in central France (Scotti & Cornet 1994). Orders of magnitude computed by Scotti and Cornet are consistent with observations.

However, more interesting are the V_P variations observed just after changes in injection flow rate. In both instances (set 3 and set 6) the anomaly that had built up during the previous injection phase is partly erased. Further, according to the detailed analysis shown in Fig. 8, the V_P anomaly disappears during a period shorter than a few hours during which no earthquake with magnitude larger than 2 has been observed. As already mentioned, Shapiro *et al.* (2002) proposed a model for the diffusion of pore pressure in a homogeneous permeable rock mass when a pressure point source is varied instantaneously and then remains constant. This sudden pressure variation occurs at distance r from the source according to the diffusion equation: $r = (4\pi\ D\ t)^{0.5}$, where D is the hydraulic diffusivity in the rock and t is time. With a diffusivity equal to 0.05 $m^2\ s^{-1}$, as measured by Shapiro at Soultz, and for a time t equal to 3 h the distance r is about 82 m. However, the size of the V_P anomalies is larger than 1000 m, at the end of set 2. Further it corresponds to an increase in velocity, not to the decrease that would have been expected from an increase in pore pressure. Hence, clearly, the change in effective stress that has induced the observed increase in V_P velocity is not associated with fluid diffusion but rather to a change in total stress. Since no earthquake with magnitude larger than 2 has been observed during this period it is proposed here that the absolute stress variation has been induced by an aseismic motion that has resulted in an increase in the spherical effective stress component $[(\sigma_1 + \sigma_2 + \sigma_3)/3 - \mathrm{P}]$ equal to a few megapascals.

Following Cornet *et al*. (2007) the natural stress field may be roughly defined by $\sigma_v = 33.8 + 0.0255(z - 1377)$ where z is depth in m; $0.95\ \sigma_v \leq \sigma_H \leq 1.01\sigma_v$; $\sigma_H \approx 0.54\ \sigma_v$. Valley & Evans (2007) come up with relationships that yield very similar values at the depths of interest. Hence, the maximum change in stress magnitude that may be anticipated when the complete shear stress is relieved reaches 45 MPa, that is, a value large enough for generating P-wave velocity variations larger than those determined by seismic tomography. This shear stress relief occurs with only small rotations in principal stress directions according to the focal plane inversion (Dorbath *et al*. 2010). Whether through shear along pre-existing fractures or through formation of a fresh shear zone, various mechanisms may be proposed to model the observed V_P variations. They all require a sound knowledge of the faults geometry away from the well. Because this information is not available yet, these mechanisms will not be discussed further here. However, it must be kept in mind that they would result with diverse consequences for anisotropy issues and that, accordingly, they may modify slightly the shapes and amplitude of the computed anomalies. The important conclusion is that results from the present tomography are unquestionably related to the stimulation and that they outline the existence of significant non-seismic large-scale deformation processes away from the well. Cornet *et al*. (1997) outlined such aseismic motions for the 1993 GPK1 simulation by direct observation of multi-centrimetric aseismic slip motion in the well.

CONCLUSION

We have coupled a tomographic method (tomoDD) with an averaging method (WAM) for analysing variations in P-wave velocity during a large-scale water injection conducted in GPK2 for stimulating the permeability in the geothermal reservoir at Soultz. During this stimulation, injection flow rate has been increased twice during the test.

By adapting the subsetting of induced microseismic events to the various water injection phases, we have obtained reliable images of P-wave velocity variations within the reservoir. They outline the existence of large rock mass volumes affected by changes in effective stresses. Some of these effective stress variations are not associated with simple water diffusion from the injection well but rather reflect the occurrence of large-scale aseismic motions in the reservoir. The modelling of these large-scale motions requires a proper knowledge of the large-scale geometry of the main faults away from GPK2, a knowledge which will become available when the recently acquired Vertical Seismic Profile (VSP) data will be fully analysed.

ACKNOWLEDGMENTS

During this work M. Calò was funded partly by ES-Geothermie thanks to J.J. Graff and partly by GEISER (FP7: 241321). We thank A. Genter and L. Dorbath for very fruitful and constructive discussions. We thank also the GEIE Exploitation Minière de la Chaleur for the hydraulic data of GPK2 stimulation. Finally we thank very sincerely Jeanot Trempert and an anonymous reviewer who helped improve the quality of the manuscript.

REFERENCES

Baria, R., Baumgärtner, J., Gérard, A. & Garnish, J. 2000. The European HDR programme: main targets and results of the deepening of the well GPK2 to 5000 m, in *Proceedings World Geothermal Congress*, Kyushu-Tohoku, Japan, pp. 3643–3652, International Geothermal Association.

Baumgärtner, J., Gérard, A., Baria, R., Jung, R., Tran-Viet, T., Gandy, T., Aquilina, L. & Garnish, J. 1998. Circulating the HDR reservoir at Soultz: maintaining production and injection flow in complete balance initial results of 1997 experiment, in *Proceedings of the 23th Workshop on Geothermal Reservoir Engineering*, Stanford, CA, 1998 January 26–28, p. 10.

Baumgärtner, J., Gérard, A. & Baria, R., 2000. Soultz-sous-Forêts: main technical aspects of deepening the well GPK2, in *Proceedings of World*

Geothermal Congress, Kyushu-Tohoku, Japan, pp. 3653–3663, International Geothermal Association.

Beauce, A., Fabriol, H., Le Masne, D., Cavoit, C., Mechler, C. & Chen, X., 1991. Seismic studies on the HDR site of Soultz-sous-Forets (Alsace, France), *Geotherm. Sci. Tech.*, **4**, 239–266.

Brun, J.P., Wenzel, F. & the ECORS-DEKORP Team, 1991. Crustal scale structure of the southern Rhine graben from ECORS-DEKORP seismic reflection data, *Geology*, **19**, 758–762.

Calò, M., 2009. Tomography of subduction zones using regional earthquakes: methodological developments and application to the Ionian slab, *PhD thesis*, EOST, University of Strasbourg (http://tel.archives-ouvertes.fr/tel-00438598/en/2).

Calò, M., Dorbath, C., Luzio, D., Rotolo, S.G. & D'Anna, G., 2009. Local earthquakes tomography in the southern Tyrrhenian region: geophysical and petrological inferences on subducting lithosphere, in *Subduction Zone Geodynamics, Frontiers in Earth Sciences*, pp. 85–99, eds Lallemand, S. & Funiciello, F., Springer-Verlag, Berlin, http://www.springerlink.com/content/p550n086507j2r17/.

Clauser, C., Griesshaber, E. & Neugebauer, H., 2002. Decoupled thermal and mantle helium anomalies: implications for the transport regime in continental rift zones, *J. Geophys. Res.,* **107**(B11), 2269–2285.

Cocherie, A., Guerrot, C., Fanning, C.M. & Genter, A., 2004. Datation U-Pb des deux faciès du granite de Soultz (Fossé Rhénan, France). *Comptes Rendus Geoscience*, **336**, 775–787.

Cornet, F.H., Helm, J., Poitrenaud, H. & Etchecopar, A., 1997. Seismic and aseismic slips induced by large scale fluid injections. *Pure appl. Geophys.*, **150**, 543–63.

Cornet, F.H., Berard, T. & Bourouis, S. 2007. How close to failure is a natural granite rock mass at 5 km depth, *Int. J. Rock Mech. Min. Sci.* **44**(1), 47–66.

Cuenot, N., Dorbath, C. & Dorbath, L., 2008. Analysis of the microseismicity induced by fluid injection in the Hot Dry Rock site of Soultz-sous-Forêts (Alsace, France): implications for the characterization of the geothermal reservoir properties, *Pure appl. Geophys.*, **165**, 797–828.

Dezayes, C., Genter, A. & Valley, B., 2010. Structure of the low permeable naturally fractured geothermal reservoir at Soultz, *Comptes Rendus Geosciences*, **343**, 7–8, 517–530, doi:10.1016/j.crte.2009.10.002.

Dorbath L., Evans, K., Cuenot, N., Valley, B., Charlety, J. & Frongeux, M., 2010. The stress field at Soultz-Sous-Forêts from focal mechanisms of induced seismic events: cases of the wells GPK2 and GPK3, *Comptes Rendus Geosciences*, doi:10.1016/j.crte.2009.12.003.

Dorbath C., Gerbault M., Carlier G. & Guiraud M., 2008. The double seismic zone of the Nazca Plate in Northern Chile: high resolution velocity structure, petrological implications and thermo-mechanical modelling, *Geochem. Geophys. Geosyst.*, **9**, doi:GC002020 10.1029/2008.

Dorbath, L., Cuenot, N., Genter, A. & Frogneux, M. 2009. Seismic response of the fractured and faulted granite of Soultz-sous-Forêts (France) to 5 km deep massive water injections, *Geophys. J. Int.*, **177**, 653–675, doi: 10.1111/j.1365-246X.2009.04030.

Dyer, B.C., 2001. Soultz GPK2 stimulation June/July 2000, *Seismic monitoring report*, Semore Seismic Report.

Elsass, P., Aquilina, L., Beauce, A., Benderitter Y., Fabriol, H., Genter, A. & Pauwels, H., 1995. Deep structures of the Soultz-sous-Forêts HDR site (Alsace, France), in *Proceedings World Geothermal Congress*, Florence, Italy, pp. 2543–2647.

Eshelby, D.J., 1957. The determination of the elastic field of an ellipsoidal inclusion and related problems, *Proc. R. Soc. Lond. Ser.*, **241**, 276–396.

Genter, A., Homeier, G., Chèvremont, P. & Tenzer, H., 1999. Deepening of GPK-2 HDR borehole, 3880–5090 m (Soultz-sous-Forêts, France), *Geological Monitoring,* Open file report BRGM/RR-40685-FR, 81.

Gérard A. & Kappelmeyer O., 1987. The Soultz-sous-Forêts project: proceedings of the first EEC/US workshop on Geothermal Hot Dry Rocks Technology, *Geothermics*, special issue, 393–399.

Hadley K., 1976. Comparison of calculated and observed crack densities and seismic velocities in Westerly granite, *J. geophys. Res.*, **81**, 3484–3494.

Hooijkaas, G.R., Genter, A. & Dezayes, C., 2006. Deep-seated geology of the granite intrusions at the Soultz EGS site based on data from 5 km-deep boreholes, *Geothermics*, **35**, 5–6, 484–506.

Kappelmeyer, O., Gérard, A., Schloemer, W., Ferrandes, R., Rummel, F. & Benderitter, Y., 1991. European HDR project at Soultz-sous-Forêts general presentation, *Geotherm. Sci. Tech.*, **2**, 263–289.

Lockner, D.A., Walsh, J.B. & Byerlee J.D., 1977. Changes in seismic velocity and attenuation during deformation of Granite, *J. geophys. Res.*, **82**, 5374–5378.

Meglis, I.L., Greenfield, R.J., Engelder, T. & Graham, E.K., 1996. Pressure dependence of velocity and attenuation and its relationship to crack closure in crystalline rocks, *J. geophys. Res.*, **101**, 17523–17533.

Menke, W. 1989. Geophysical data analysis, in *Discrete Inverse Theory*, Academic Press, San Diego, CA.

Nur, A., 1987. Seismic rock properties for reservoir descriptions and monitoring, in *Seismic Tomography-With Applications in Global Seismology and Exploration Geophysics*, eds Nolet, G. and Reidel, D., pp. 203–237, Norwell, MA, USA.

Nur, A. & Simmons, G., 1969, Stress-induced velocity anisotropy in rock: an experimental study, *J. geophys. Res.*, **74**, 6667–6674.

Reuschlé, T, Haore, S.G. & Darot M., 2006. The effect of heating on the microstrucutral evolution of La Peyratte granite deduced from acoustic velocity measurements, *Earth planet. Sci. Lett.*, **243**, 693–700.

Scotti O. & Cornet F.H., 1994; In situ evidence for fluid induced aseismic slip events along fault zones, *Int. J. Rock Mech. Min.*, **31**(4), 347–358.

Schnaebele, R., Hass, J.-O. & Hoffmann, C.R., 1948. Monographie géologique du champ pétrolifère de Pechelbronn, *Mém. Serv. Carte Géol. Alsace Lorraine*, **254,** 1–7.

Shapiro, S.A., Rothert, E., Rath, V. & Rindschwenter, J., 2002. Characterization of fluid transport properties of reservoirs using induced microseismicity, *Geophysics*, **67,** 212–220.

Shelly, D.R., Beroza, G.C., Zhang, H., Thurber, C.H. & Ide S., 2006. High resolution subduction zone seismicity and velocity structure beneath Ibaraki Prefecture, Japan, *J. geophys. Res.*, **111**, B06311, doi:10.1029/2005JB004081.

Stanchits, S.A., Lockner, D.A. & Pomonarev, A.V., 2003. Anisotropic changes in P-wave velocity and attenuation during deformation and fluid infiltration in granite, *Bull. seism. Soc. Am.*, **93(4)**, 1803–1822.

Stussi, J., Cheilletz, A., Royer, J., Chevremont, P. & Ferraud, G., 2002. The hidden monzogranite of Soultz-sous-Forets (Rhine Graben, France), *Mineralogy, Petrology and Genesis, Géologie de la France*, **1**, 45–64.

Thurber, C., Roecker, S., Roberts, K., Gold, M., Powell, L. & Rittger, K., 2003. Earthquake locations and threedimensional fault zone structure along the creeping section of the San Andreas fault near Parkfield, CA: preparing for SAFOD, *Geophys. Res. Lett.*, **30**(3), 1112, doi:10.1029/2002GL016004.

Toomey, D.R. & Foulger, G.R., 1989. Tomography inversion of local earthquake data from the Hengill Grensdalur central volcano complex, Iceland, *J. geophys. Res.*, **94** B12, 17 497–17 510.

Valley, B. & Evans, K.F., 2007. Stress State At Soultz-Sous-Forêts to 5 km depth from wellbore failure and hydraulic observations, in *Proceedings 32nd Workshop on Geothermal Reservoir Engineering,* Stanford University, Stanford, CA, 2007 January 22–24.

Waldhauser, F. & Ellsworth, W.L., 2000. A double-difference earthquake location algorithm: method and application to the Hayward fault, *Bull. seism. Soc. Am.*, **90**, 1353–1368.

Weidler, R., Gérard, A., Baria, R., Baumgartner, J. & Jung, R., 2002. Hydraulic and micro-seismic results of massive stimulation test at 5 km depth at the European Hot-Dry-Rock test site Soultz, France, in *Proceedings 27th Workshop on Geothermal Reservoir Engineering*, pp. 95–100, Stanford, CA, USA.

Zhang, H., 2003. Double-difference seismic tomography method and its applications, *PhD thesis*, Univ. of Wisconsin, Madison.

Zhang, H. & Thurber, C.H., 2003. Double-difference tomography: the method and its application to the Hayward fault, California, *Bull. seism. Soc. Am.*, **93**, 1175–1189.

Zhang, H., & Thurber, C.H., 2007. Estimating the model resolution matrix for large seismic tomography problems based on Lanczos bidiagonalization with partial reorthogo nalization, *Geophys. J. Int.*, **170**, 337–345, doi:10.1111/j.1365-246X.2007.03418.x.

Zhang, H., Thurber, C.H. & Bedrosian, P., 2009. Joint seismic velocity inversion around safod, *Geochem. Geophys. Geosyst.* **10**(11), Q11002, doi:10.1029/2009GC002709

Zhao, D., Hasegawa, A. & Kanamori, H., 1992. Tomographic imaging of P and S wave velocity structure beneath northeastern Japan, *J. geophys. Res.*, **97**, 19 909–19 928.

Ziegler P., 1992. European cenozoic rift system, *Tectonophysics*, **2008**, 91–111.

APPENDIX A

The WAM method (Calò 2009; Calò *et al*. 2009) is a post-processing technique that may be used with any tomographic inversion code. With the WAM method the final velocity values are the weighted mean of velocities obtained after performing numerous inversions. In this work each final tomogram is the result of the merging of 15 models previously calculated with tomoDD.

In this study we used the DWS (Toomey & Foulger 1989) as the weighting factor, for it is directly related to the experimental information used to determine the velocity during the *i*th inversion. The DWS yields a measure of the density of rays that pass near a gridpoint. It is weighted according to how close each ray passes to the node and is therefore superior and more representative than the commonly quoted 'Hit Matrix', which is merely a count of the number of rays that pass close to the gridpoint.

A large DWS indicates that the velocity at the gridpoint is based on a large body of data. Zhang *et al*. (2009) and Zhang & Thurber (2007) show that the DWS distribution is a good indicator of the resolution distribution. However any 'quality parameter; (e.g. spread function, diagonal elements; Menke 1989) may be used as well as weighting factor. Each V_P and DWS distribution relative to an *i*th inversion is resampled into a dense fixed grid (WAM grid) using the same interpolation law as tomoDD to determine the continuous velocity model between nodes of the inversion grid.

Equations used for determining the weights (w_i) for the velocity values into the fixed grid are

$$\text{if } \ \mathrm{DWS}_i = 0 \Rightarrow w_i = 0,$$

$$\text{if } \ \mathrm{DWS}_i \leq \mathrm{LIM} \Rightarrow w_i = \frac{\mathrm{LIM}}{\mathrm{COST}},$$

$$\text{if } \ \mathrm{DWS}_i > \mathrm{LIM} \Rightarrow \ w_i = \overline{\mathrm{DWS}_i}\,\frac{(\mathrm{DWS}_i - \mathrm{LIM})}{(\mathrm{DWS}_{i\,\max} - \mathrm{LIM})} + \mathrm{LIM},$$

where $\mathrm{DWS}_{i\max}$ and $\overline{\mathrm{DWS}_i}$ are the maximum and averaged DWS values in the *i*th node, respectively, LIM is a threshold of DWS defined to pick out the values where the velocity estimates is considered to be reliable. The parameter COST is a constant, which is empirically optimized. We estimated that a value of 2 for the LIM/COST ratio is reasonable for most of the tests performed (see Appendix A). The DWS was set to zero at nodes where no velocity estimate could be assigned. The LIM value was fixed at a DWS threshold equal to 10 to include the maximum number of nodes inverted during each inversion (Zhang 2003).

Isosurface DWS = LIM encloses the volume resolved with the final tomographic model. We use the same weights both for calculating the mean velocity and for determining the WSTD of the velocities at each node.

The DWS(*i,j,k*) at the (*i,j,k*)-node of the WAM grid has been determined with the following relationship:

$$\mathrm{DWS}(i,\,j,\,k) = \frac{\sum_{i=1}^{n} w_i \mathrm{DWS}_i(i,\,j,\,k)}{\sum_{i=1}^{n} w_i},$$

where w_i have the weights previously defined.

This simple weighting scheme emphasizes velocity values that are the most reliable. Indeed they are constrained by more experimental information and they contribute the most significantly to the mean velocity estimate at the WAM grid nodes.

In this study the *P*-wave velocity field is calculated for all the nodes for which DWS is greater than 10. This value should be considered a little bit optimistic to estimate the best resolved area. Nevertheless in our study we decided to include the largest number of nodes for which a velocity value is calculated following Zhang (2003). However, to assess the reliability of our results and to show the resolution power of the data and method we build a synthetic model characterized by a low *P*- velocity rectangular prism of –5 per cent with respect to the initial 1-D velocity model (Fig. 1). The body is placed around the open-hole section of GPK2 and has dimensions of $0.75 \times 0.75 \times 1$ km^3 in the *x*-, *y*- and *z*-directions, respectively. This model should be considered as an approximation of the velocity structures that have been observed for most of the sets and allows us to perform a synthetic test close to the Restoration–Resolution test (Zhao *et al*. 1992). With the same configuration of earthquakes and stations as in the real inversion, we calculate synthetic travel times for four representative datasets.

We selected for the test the following sets: (1) Set N 1 that contains 300 events and corresponds to the most concentrated seismic cloud of our database; (2) Set N 5 including only 240 events and corresponding to the smallest data set; (3) Set N 10 containing 480 events; it represents one of the most representative sets in terms of shape of the seismic cloud and (4) Set N 14, containing 450 events corresponding to the most spread seismic cloud.

For each data set we simulate the same possible picking errors by adding a vector of random errors with standard deviation equal to 0.01 s. The 1-D initial model is then used as starting velocity distribution for the inversion of the perturbed synthetic databases.

Fig. 1 shows the results after the inversion of the synthetic data using only the tomoDD code for the four tests. Two velocity isovalues (5.35 km s^{-1} and 5.8 km s^{-1}) characterizing the shape of the rectangular prism (bold lines) are also reported. The low V_P anomaly is roughly recovered in the region around the foci and the part of the model, which is above it does not exhibit any strong artefact for all the sets. For better estimating the reconstruction capability of the true velocity structures we calculate the mean restoration of the velocities in the investigated volume.

$$R(i,\,j,\,k,\,) = 100\left(1 - \frac{|x_t(i,\,j,\,k) - x_v(i,\,j,\,k)|}{|x_i(i,\,j,\,k) - x_v(i,\,j,\,k)|}\right),$$

where $x_t(i,j,k)$, $x_v(i,j,k)$ and $x_i(i,j,k)$ are, respectively, the final, the 3-D true and the 1-D initial velocity values at node (*i,j,k*). The mean restorations are ranging, for the four tests, from 49 to 58 per cent for the whole illuminated volume (from the surface down to a depth of 5.8 km), from 54 to 63 per cent for the deeper part (2.5–5.8 km of depth) and from 36 to 55 per cent when only the low V_P anomaly is considered.

These tests highlight that double difference tomographic method applied to small and very concentrated data sets is able to recover with satisfactory reliability the velocity structures in the regions near and above the events.

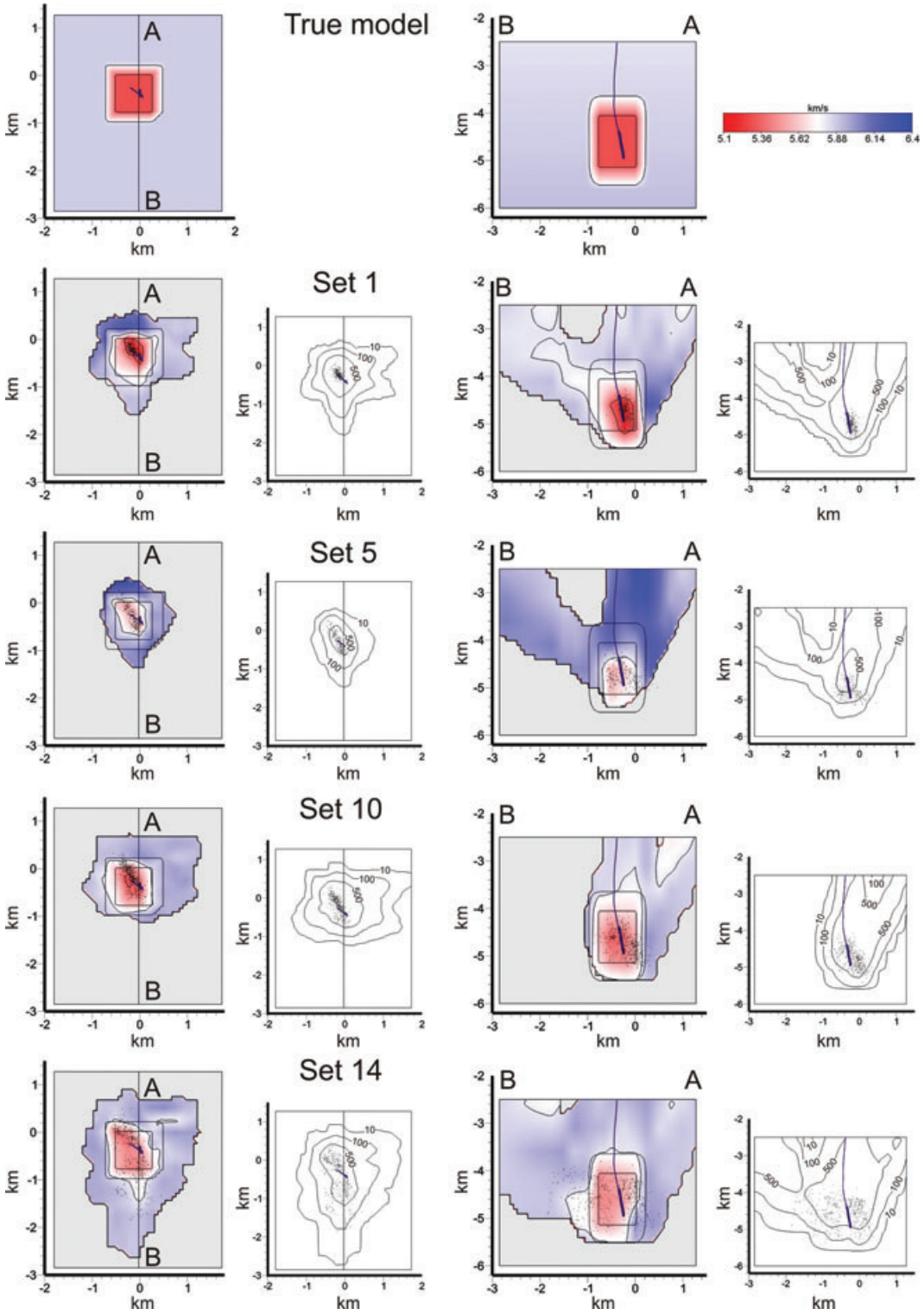

Figure A1. First row: Map view at 4.6 km depth and vertical section of the V_P model used to calculate the synthetic traveltimes. Below: map view and cross-sections of the models obtained with tomoDD only for the four representative sets. The bold lines are the isovalues at 5.35 km s^{-1} and 5.8 km s^{-1} characterizing the true velocity anomaly. The corresponding isocontour of DWS distributions are reported on the right-hand side.

Fig. 2 shows the velocity model obtained with the WAM method for the four sets. The corresponding mean restoration range from 71 to78 per cent for the whole illuminated volume, 83 to 86 per cent for the deeper part and 68 to 76 per cent when only the low V_P anomaly is considered. We have to remind that these models are obtained by the weighted mean of 15 different velocity models previously obtained with the schemes described earlier. With this method the velocity estimate at each node is determined by giving more weight to the velocities calculated with the highest (and then more reliable) values of DWS. With these tests we demonstrate that the method

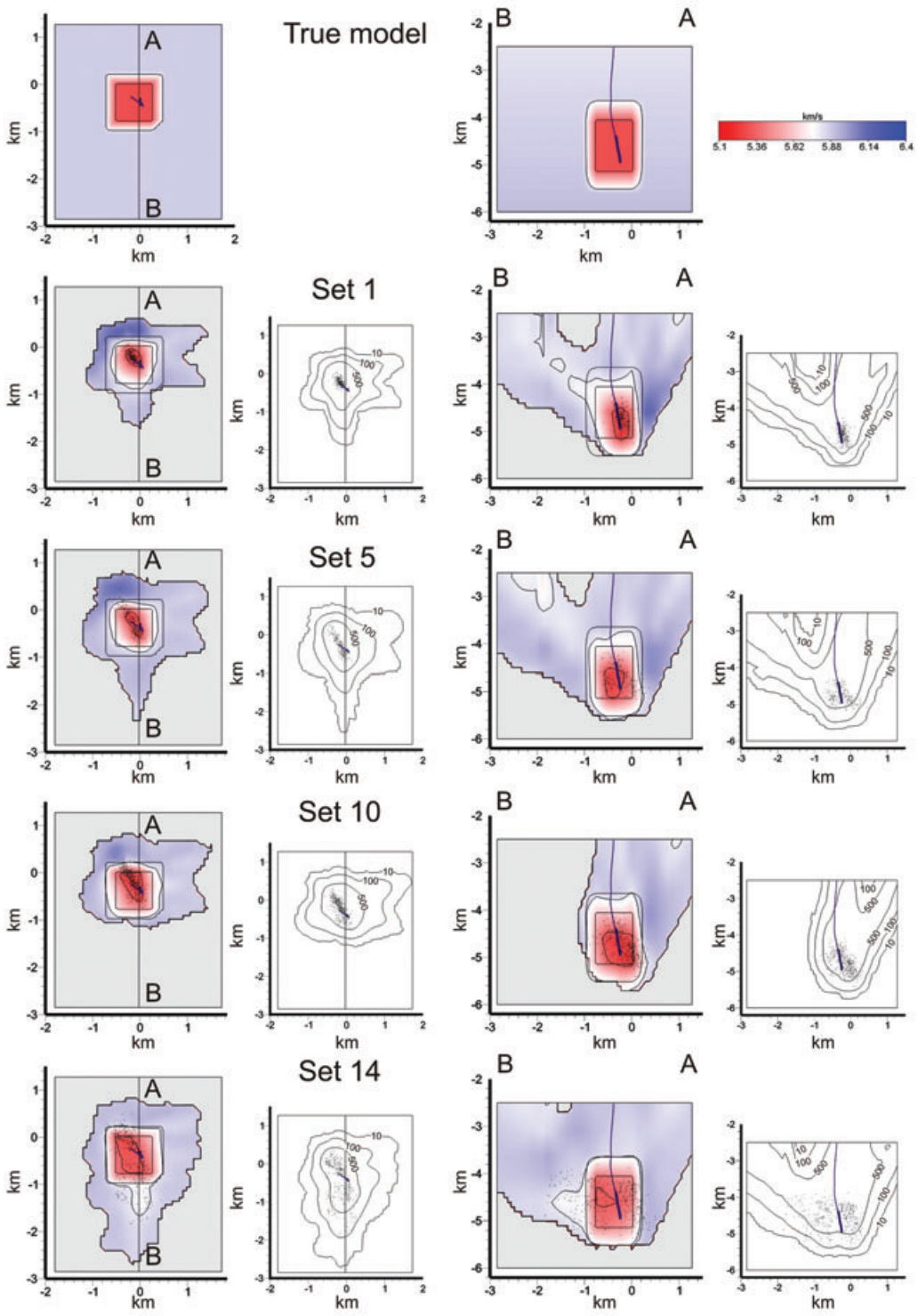

Figure A2. First row: Map view at 4.6 km depth and vertical section of the V_P model used to calculate the synthetic traveltimes. Below: map view and cross-sections of the models obtained with the method tomoDD plus WAM for the four representative sets. The bold lines are the isovalues at 5.35 km s^{-1} and 5.8 km s^{-1} characterizing the true velocity anomaly. The corresponding isocontour of DWS distributions are reported on the right-hand side.

used (tomoDD plus WAM) is able to recover at least about 70 per cent of the velocity structures in the volume where DWS > 10. The velocity isocontour at 5.8 km s^{-1} shows that the shape of the prism is well recovered. It is worth noting that we have used the most representative sets of our database for performing these tests, to identify explicitly the resolution that has been reached with the applied method. Since the events observed during the stimulation are located always within the same region and did not migrate appreciably during the whole stimulation test, we can assume that these results are well representative of the reconstruction powers. All the other sets, that are much larger, guarantee an even better reliability.

APPENDIX B

The WAM method allows calculating a WSTD of the velocity estimates. The WSTD is calculated directly using the velocity distributions used to build the WAM and with the same weighting scheme as to obtain the final velocity. It describes the variability of the models that have been used and it provides an estimation of the dependence of the single models to the input parameters. Thus a larger value of WSTD suggests a lager dependence of the models to the input parameters, therefore a lower reliability of the velocity estimates. Furthermore, as demonstrated by some tests (Calò 2009), the WSTD is directly linked to the restoration capability of a corresponding traditional restoration test and

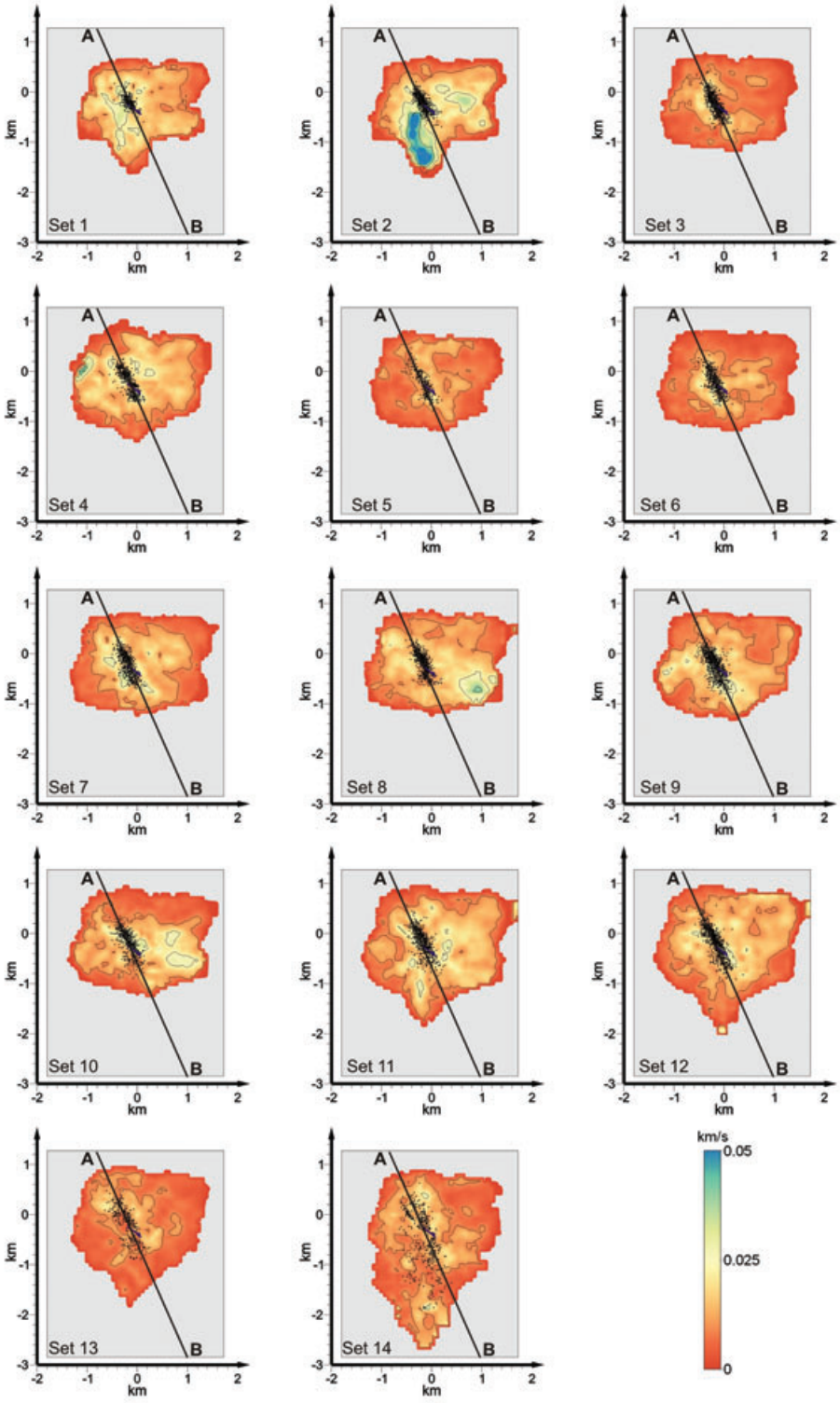

Figure B1. Horizontal slices at 4.6 km of depth of the weighted standard deviations (WSTD) for the 14 tomograms.

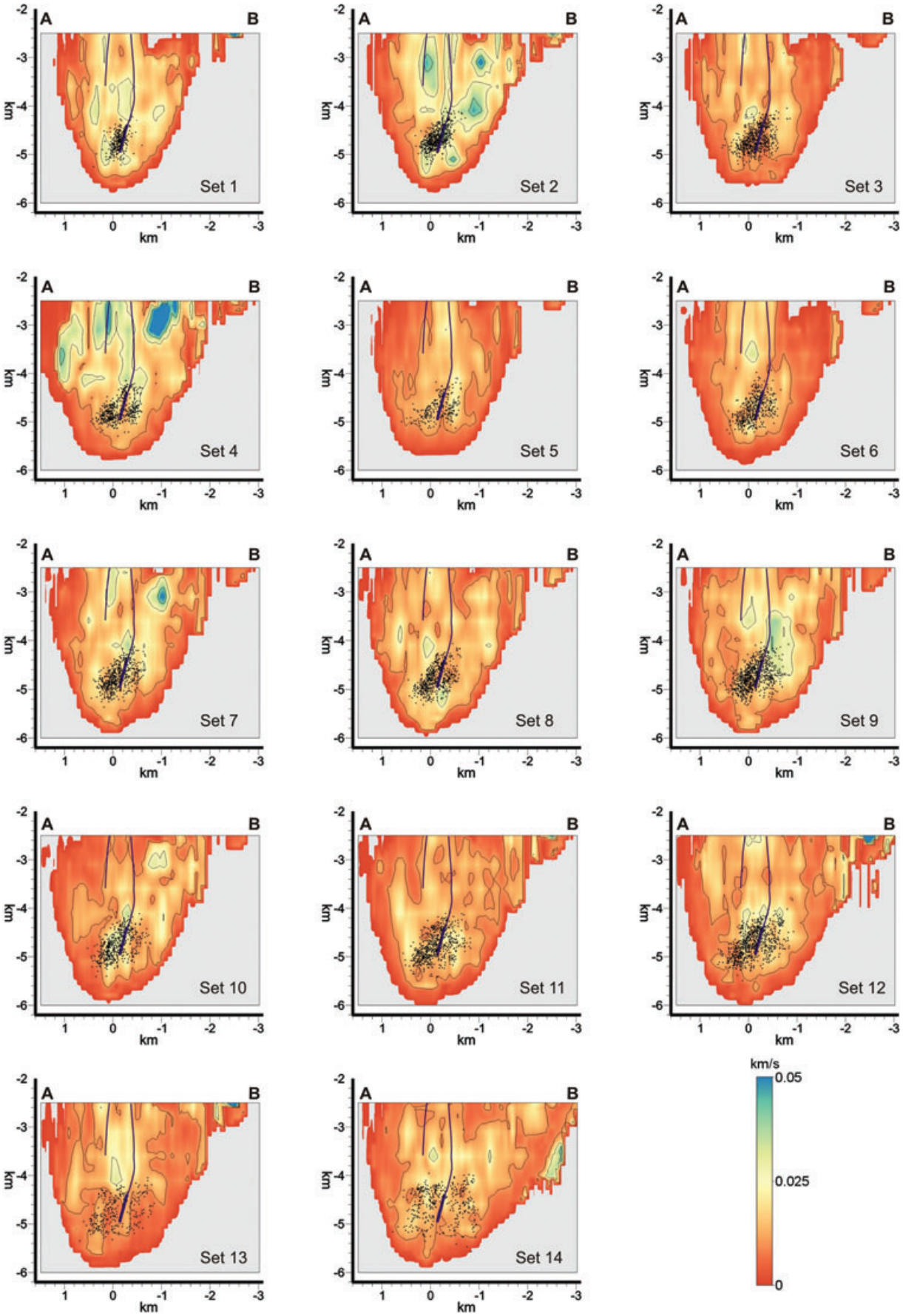

Figure B2. Vertical sections of the weighted standard deviations (WSTD) for the 14 tomograms.

they may be used as parameter for estimating the reliability of the model.

We assessed that a high spatial coherence between anomalies and higher WSTD suggests the presence of bias in the velocity structures. Figs 1 and 2 display the horizontal and vertical sections of the experimental WSTD for the fourteen models, respectively.

An example of the spatial coherence between WSTD and V_P anomaly (with V_P values greater than 0.45 km s^{-1}) has been observed for the model of the set 2 (Fig. 5) It is confined close to the boundary of the well-resolved domain and it is spatially correlated with the highest values for WSTD (Fig. 1, Appendix B). Hence we cannot exclude that in this case this large value is caused by some instabilities in the velocity model.

However, the WSTD are smaller than 0.025 km s^{-1} for most of the 14 sets. They reach 0.05 km s^{-1} in few areas and this only for some of the sets. These values are significantly lower than the amplitude of the velocity variation observed in the area, and even considering an error bar of 2σ ($\sim$95 per cent confidence interval), the reliability of the anomalies remains very high. Furthermore the absence of spatial correlation between the highest WSTD and velocity anomalies ensures the low dependence of the velocity models on the initial parameters and therefore supports the reliability of the results.